frontiers in Astronomy and Space Sciences

TYPE Original Research
PUBLISHED 19 June 2026
DOI 10.3389/fspas.2026.1814323

The influence of opacity on inferred MHD wave signatures in the lower solar atmosphere

Samuel J. Skirvin[1,2]*, Samuel D. T. Grant[2], David B. Jess[2,3], Ryan J. Campbell[2], Shahin Jafarzadeh[2], Mika V. Kontiainen[2,4], Michele Berretti[5,6], Timothy J. Duckenfield[2], Glen Chambers[2], Marco Stangalini[7] and Luc Rouppe van der Voort[8,9]

[1]School of Engineering, Physics and Mathematics, Northumbria University, Newcastle Upon Tyne, United Kingdom, [2]Astrophysics Research Centre, School of Mathematics and Physics, Queen's University Belfast, Belfast, United Kingdom, [3]Department of Physics and Astronomy, California State University Northridge, Northridge, CA, United States, [4]Institute of Astronomy, University of Cambridge, Cambridge, United Kingdom, [5]University of Trento, Trento, Italy, [6]Department of Physics, University of Rome Tor Vergata, Rome, Italy, [7]ASI, Italian Space Agency, Rome, Italy, [8]Institute of Theoretical Astrophysics, University of Oslo, Oslo, Norway, [9]Rosseland Centre for Solar Physics, University of Oslo, Oslo, Norway

OPEN ACCESS

EDITED BY
Abhishek Kumar Srivastava,
Indian Institute of Technology (BHU), India

REVIEWED BY
Diana Besliu-Ionescu,
Astronomical Institute of the Romanian Academy, Romania
Amoré Nel,
South African National Space Agency, South Africa

*CORRESPONDENCE
Samuel J. Skirvin,
samuel.j.skirvin@northumbria.ac.uk

RECEIVED 20 February 2026
REVISED 08 May 2026
ACCEPTED 25 May 2026
PUBLISHED 19 June 2026

CITATION
Skirvin SJ, Grant SDT, Jess DB, Campbell RJ, Jafarzadeh S, Kontiainen MV, Berretti M, Duckenfield TJ, Chambers G, Stangalini M and Rouppe van der Voort L (2026) The influence of opacity on inferred MHD wave signatures in the lower solar atmosphere. *Front. Astron. Space Sci.* 13:1814323. doi: 10.3389/fspas.2026.1814323

Magnetohydrodynamic wave activity in small-scale magnetic structures, such as solar pores, provides key insights into energy transport in the lower solar atmosphere. This study presents high-resolution observations of ten solar pores contained within a 43×43 Mm^2 field of view, obtained with the CRISP instrument at the Swedish 1-m Solar Telescope. We investigate the temporal behaviour of the line-of-sight velocity (v_{LOS}) and magnetic field (B_{LOS}) oscillations within the pore structures. Using SIR inversions, we analyse the oscillatory signals at multiple optical depths (log τ levels) to assess how variations in geometric height (z) and temperature relate to the observed B_{LOS} fluctuations. Our results reveal that higher-frequency oscillations (6 mHz) exhibit strong coherences with in-phase fluctuations between B_{LOS} and z across atmospheric layers, consistent with upward-propagating magneto-acoustic waves. In contrast, coherent lower-frequency oscillations display significant phase differences, which may arise from opacity effects contaminating the inversion response. These findings highlight the importance of accounting for opacity effects when interpreting magnetic oscillations, with direct implications for forthcoming high-precision magnetic diagnostics from facilities such as DKIST.

KEYWORDS
magnetohydrodynamics, MHD waves, solar active region magnetic fields, solar oscillations, solar photosphere

1 Introduction

The solar atmosphere is replete with oscillations interpreted as the presence of magnetohydrodynamic (MHD) waves (Jess et al., 2015; Van Doorsselaere et al., 2020; Jess et al., 2023; Morton et al., 2023), which are important for the dynamical coupling, energy transport and potential plasma heating across the solar atmosphere. Solar pores, regions of stronger magnetic field often related to the formation or breaking of a sunspot (Garcia de La Rosa, 1987), typically possess mean field strengths of 1200 – 1600 G and mean inclinations of 30° (Sobotka, 2003; Campos Rozo et al., 2023). Their smaller size compared to sunspots permits a greater influence from localised drivers such as granular buffeting (Riedl et al., 2021), resulting in the ubiquitous generation of global MHD wave modes. Solar pores have been shown to support various MHD modes such as sausage modes (Dorotovič et al., 2008; Morton et al., 2011; Grant et al., 2015; Keys et al., 2018; Gilchrist-Millar et al., 2021; Grant et al., 2022), in addition to higher order kink modes and fluting modes (Jafarzadeh et al., 2024).

Capturing signatures of magnetic field oscillations has been of great interest for decades, however, two primary factors have prohibited detailed study; the instrumental sensitivity required to detect incremental polarimetric signatures (Bailén et al., 2023) and the need to develop robust inversion techniques to extract the magnetic field information (de la Cruz Rodríguez and van Noort, 2017). As advancements have been made on both fronts, observational campaigns have begun to reveal the oscillatory nature of the strong magnetic fields in the lower atmosphere (Fujimura and Tsuneta, 2009; Houston et al., 2018; Joshi and de la Cruz Rodríguez, 2018; Nelson et al., 2021; Stangalini et al., 2021a; Murabito et al., 2021). These works were able to recover behaviours similar to those seen in velocity data, such as the predominance of the p-mode spectrum, although some discrepancies seemed to indicate that these atmospheric parameters were not mirroring one another. For example, Stangalini et al. (2021b) provided the first indication of a disconnect between velocity and magnetic field. A comparison between circular polarisation (deployed as a proxy of magnetic field) and velocity revealed distinctive power spectra in a magnetic pore. Their peak-frequencies were offset, with line-of-sight (LOS) velocity showing increased higher frequency power. The implications of magnetic and velocity fields displaying distinct wave energetics are vast, implying that magnetic oscillations could hold novel truths about the solar atmosphere. It is therefore vital to study this disconnect in greater detail.

A recent analysis by Felipe and Socas-Navarro (2023) explored the extent to which NLTE inversions accurately recover chromospheric oscillations produced by wave propagation, finding that height-dependent opacity effects significantly modify the retrieved velocity and temperature oscillations and become especially important for frequencies exceeding 9 mHz. Moreover, a recent observational study by Grant et al. (2022) examined the propagation of coherent magnetohydrodynamic waves across multiple solar magnetic pores, finding ubiquitous slow sausage-mode oscillations in the photosphere that remain coherent at low heights but become decorrelated in the chromosphere, with evidence of power amplification near 5 mHz and complex height-dependent wave morphology.

In this study, we examine high-resolution data obtained from the Swedish Solar Telescope to investigate the influence of opacity, if any, on the observed solar p-mode spectrum and search for further evidence of MHD wave propagation across a number of solar pores. The paper is structured as follows: in Section 2 we outline the observations used in the current work, and the procedure of identifying the pores and their properties. Section 3 highlights the results of the wave analysis on the SIR inversions. Finally, in Section 4 we provide a brief summary of our results, implications for interpreting oscillations in the solar photosphere and necessary avenues of future work.

2 Observations and data processing

The data presented here is an observational sequence obtained with the 1-m Swedish Solar Telescope (SST; Scharmer et al., 2003; 2019) during 08:52 – 09:45 UT on 2016 September 05. The region of interest was active region NOAA 12585, with the field-of-view (FoV) centred around a group of magnetic pores at heliocentric co-ordinates ($-172''$, $22''$), corresponding to the cosine of an observing angle of $\mu = 0.98$. The CRisp Imaging SPectropolarimeter (CRISP; Scharmer et al., 2008) was utilised to provide spectro-polarimetric imaging data of the Fe I 6,301 and 6,302 Å line pair sampling 16 non-equidistant wavelength steps from −1.17–0.08 Å around the Fe I 6,302 Å line-core. The CRISP instrument imaged a $59'' \times 59''$ (approximately 43×43 Mm^2) region of the solar disk (see Figure 1), with a spatial sampling of $0.059''$ (43 km) per pixel and temporal cadence of 32.2 s for a total of 98 scans. Seeing remained good throughout, with data fidelity improved through the use of high-order adaptive optics (Scharmer et al., 2003), alongside processing with the CRISPRED pipeline (de la Cruz Rodríguez et al., 2015), Multi-Object Multi-Frame Blind Deconvolution (MOMFBD; Van Noort et al., 2005) image restoration and image destretching.

The data was inverted using the Stokes Inversion based on Response functions (SIR; Ruiz Cobo and del Toro Iniesta, 1992) code under the assumption of local thermodynamic equilibrium (LTE) in order to infer the physical parameters of the atmosphere for the full field-of-view. Each Stokes vector was inverted multiple times using randomised initial values for magnetic field strength, B, line-of-sight velocity, v_{LOS}, magnetic inclination, γ, and magnetic azimuth, ϕ, with only the best-fit solution retained. This reduces sensitivity to initial conditions and reduces the probability of convergence to local, as opposed to global, minima. Elemental abundances were adopted from Asplund et al. (2009). One inversion cycle was employed with five nodes in temperature, three nodes each in B and v_{LOS}, two in γ, and one in ϕ.

We compute the inversions at two different optical depths corresponding to $\log\tau = -1$ and $\log\tau = -2$. This is because the Fe I 6,301 Å and 6,302 Å line pair Stokes V sensitivity to B_{LOS} is broad, but typically peaks within the range $\log\tau = [--1.3: -1.7]$ (Quintero Noda et al., 2021). Therefore, these optical depths are representative of the most accurately inferred B_{LOS} signals and are utilised to provide a physical picture of where the B_{LOS} signal originates in pores observed in the SST FoV.

2.1 Pore identification

Solar pores are regions of strong magnetic field in the Sun's photosphere, hence they appear dark in intensity maps due to suppressed plasma convection. At each time step, the continuum intensity was normalised with respect to the mean intensity of the quiescent Sun, I_{QS}, defined as sub-field where the LOS magnetic field strength was <50 G. The normalised frames were combined to construct a mean continuum intensity frame (Figure 1). The

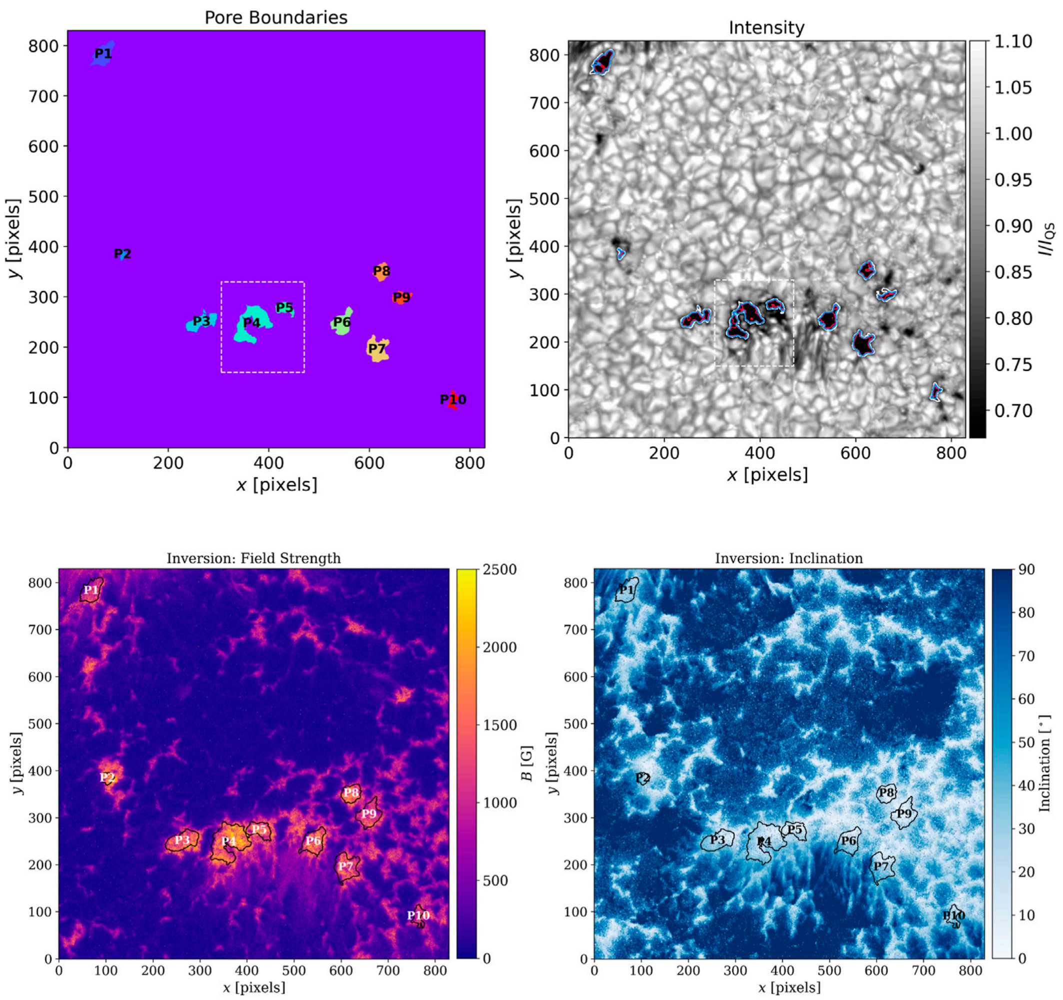

FIGURE 1
Reduced field of view for the region of interest. (Top Left) Labelled maximum pore boundaries P1–P10. (Top Right) Mean continuum intensity with regions identified as belonging to a pore at any point in the time series (white), in the mean (blue), and throughout the time series (red). The dashed white box is the active region within which a different intensity threshold is used to minimise interference from the emerging penumbral region and spurious coalescence of the neighbouring pores. (Bottom left) Total magnetic field strength obtained from the SIR inversion. (Bottom right) Inclination angle at the initial time of observation from the SIR inversion.

maximum boundaries for pore candidates (white contours) were then defined as contiguous groupings of pixels that at some point in the time series satisfy $I/I_{QS} \leq 0.6$ in the active region (dashed white box) and $I/I_{QS} \leq 0.7$ elsewhere. To ensure their suitability for wavelet analysis, only those pore candidates were retained for which a corresponding structure greater than 100 pixels in area could be identified in the mean continuum intensity frame (blue contours). The resulting pore boundaries were labelled P1–P10 from left to right, and the pores in each frame of time series were identified as groupings of pixels satisfying the intensity thresholds within the established maximum pore boundaries. To rule out potential false signals due to incoherent oscillations within the pores, the pores with non-vanishing permanent areas (1, 3, 4, 6, 7, 8, 9) were chosen for further analysis and are discussed in the following sections. The three excluded pores (P2, P5, P10) were omitted as they did not maintain coherent structures which were large enough to be confidently traced throughout the duration of the observation. For example, P5 temporarily merges with P4, while P10 appears only intermittently above the intensity threshold. P2, the largest of the excluded pores, was found to exhibit an energy spectral density comparable to the analysed pores (e.g., P8, displayed in Figure 2), suggesting the selection criterion does not introduce a systematic bias in the observed wave statistics.

2.2 Pore properties

The pore area, ^{v}LOS, magnetic field strength, magnetic field inclination and temperature were calculated from the SIR inversions at $\log(\tau) = -1$. Note that magnetic field is directed into the Sun (i.e., $B_{LOS} < 0$) so the inclination angles have been calculated using '180–inclination'.

To determine the pore morphology, we utilized the binary map of the maximum pore boundaries where

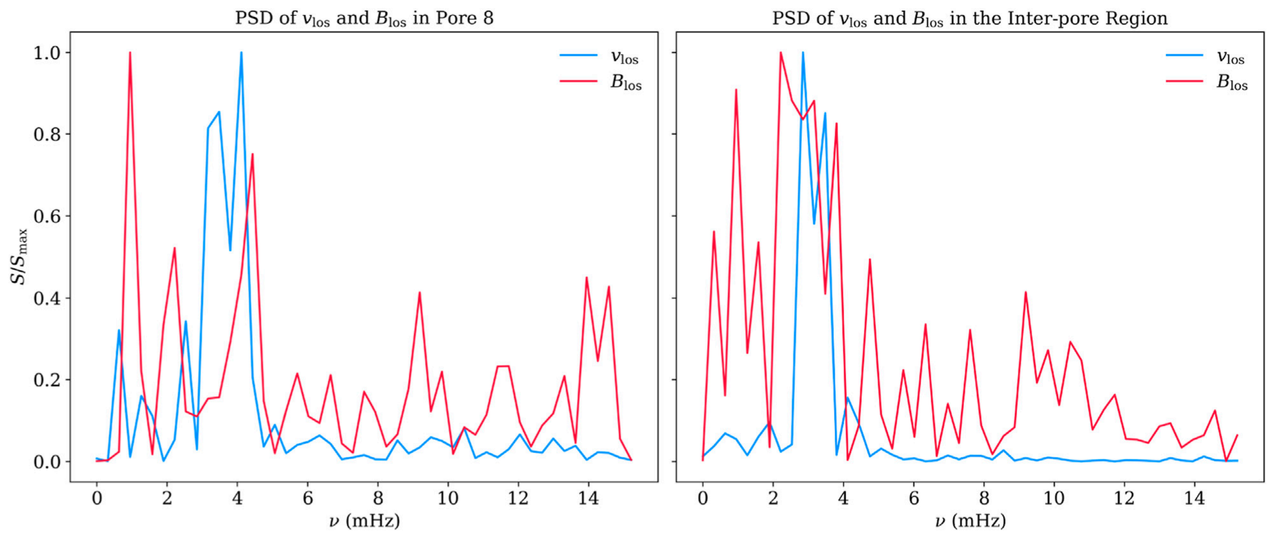

FIGURE 2
Normalised power spectral density as calculated from the detrended and apodised ^{v}LOS (blue) and B_{LOS} (red) time series, determined from the SIR inversion, for pore 8 (left) and the inter-pore region (right) identified as being free of pores for the duration of the time series.

TABLE 1 **Average properties of the seven pores identified at the solar surface and used for further analysis.**

Pore	Area (Mm^2)	LoS velocity (km s^{-1})	Magnetic field (G)	Inclination (°)	Temperature (*K*)
Pore 1	1.48 ± 0.40	0.47 ± 0.46	1137 ± 225	28.0 ± 7.6	4786 ± 105
Pore 3	2.17 ± 0.31	0.57 ± 0.46	1407 ± 373	24.4 ± 10.8	4744 ± 114
Pore 4	4.06 ± 0.43	0.44 ± 0.33	1812 ± 465	20.2 ± 19.3	4552 ± 97
Pore 6	1.76 ± 0.33	0.52 ± 0.47	1336 ± 396	21.2 ± 15.1	4766 ± 124
Pore 7	2.26 ± 0.22	0.56 ± 0.53	1218 ± 314	25.4 ± 11.2	4579 ± 80
Pore 8	1.31 ± 0.13	0.69 ± 0.74	1430 ± 397	17.5 ± 28.4	4813 ± 97
Pore 9	1.38 ± 0.35	0.73 ± 0.67	1219 ± 307	15.9 ± 18.2	4774 ± 154

the barycentre of each individual pore was found using `scipy.ndimage.center_of_mass` and both barycentric minimum circumscribed and maximum inscribed circles fitted to the pore pixels (Sui and Zhang, 2012). After conducting the SIR inversions, we can use the permanent pore pixels to determine the average line of sight velocity, magnetic field strength, magnetic field inclination and plasma temperature within each pore, where the values are outlined in Table 1.

3 Analysis and discussion

In this work, we wish to study whether opacity or geometric effects can contribute to the apparent coherence between ^{v}LOS and B_{LOS} signals in a group of solar pores, and may be incorrectly interpreted as real magnetic oscillations (i.e., MHD waves). Moreover, we wish to understand the effect, if any, of opacity effects modifying the observed power spectrum.

3.1 Wave activity

In order to analyse wave activity in the identified pores, the ^{v}LOS and B_{LOS} time series for each pore with non-vanishing permanent areas (e.g., pores 1, 3, 4, 6, 7, 8, 9), were obtained using the binary maps, detrended with a linear fit, and apodised using a Tukey window with taper fraction $\alpha = 0.1$. This yielded appropriate time series for Morlet wavelet analysis, an example of which is shown in Figure 3 for the ^{v}LOS signal of pore 8. The duration of wave activity at 95% significance for each frequency/period was calculated as a fraction of the total length of the time series. Statistical significance was assessed against a red noise (AR(1)) background spectrum using the method of Torrence and Compo (1998), where the lag-1 autocorrelation was estimated from the data. We interpret only periods for which at least three oscillation cycles are supported outside the cone-of-influence (COI). For a Morlet wavelet, the COI e-folding time scales as $\sqrt{2}\,s_w$, which motivates excluding periods approaching the total duration T of the time series; in practice we adopt an effective maximum reliable period of order $P_{max} \sim T/(3\sqrt{2})$.

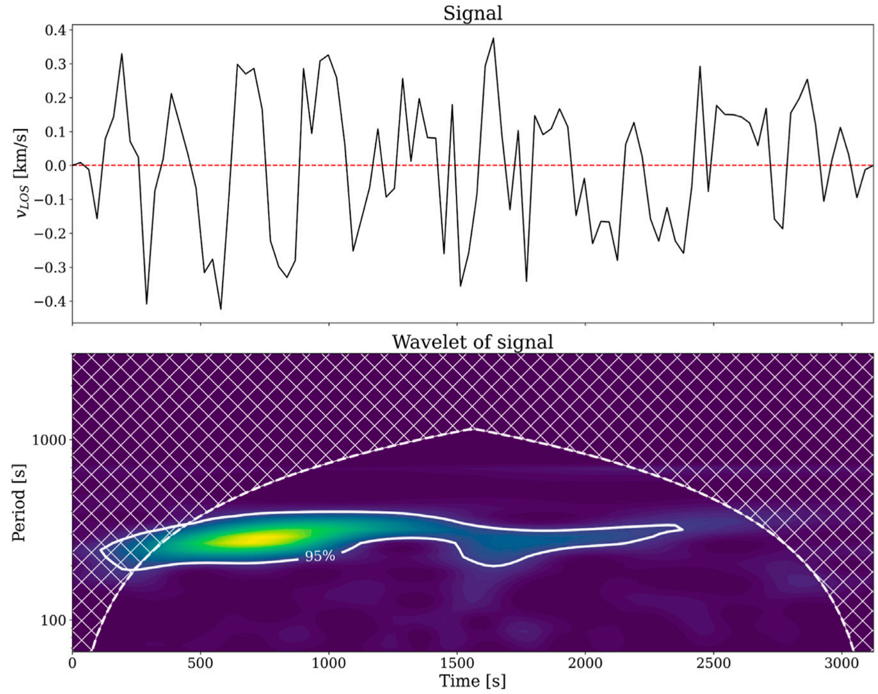

FIGURE 3
Wavelet power spectrum of ^{v}LOS time series for P8. Prior to the wavelet transform, the time series was detrended with a 3rd-order polynomial and apodised with a 90% tapered cosine filter.

Using the detrended and apodised ^{v}LOS and $B_{\rm LOS}$ time series, the power spectral density (PSD) for each pore was obtained following Grant et al. (2022). We performed a fast Fourier transform on the detrended time series. The resulting Fourier transform $X(f)$ (complex amplitude) was used to calculate the power spectral density given by Equation 1:

$$S(f) = \frac{2|X(f)|^2}{\delta v}, \tag{1}$$

where S represents the PSD and δv is the frequency sampling. As an example, Figure 2 displays the resulting PSD for P8 and the inter-pore region, while the distribution for all pores is shown in Figure 4. It is clear that the ^{v}LOS signal in both the pore and interpore regions, displays a strong power around 3 mHz. The $B_{\rm LOS}$ signal in the interpore region also peaks around a similar frequency, however, within the pore, there is significant power at both lower and higher frequencies for $B_{\rm LOS}$.

3.2 Phase differences

To determine whether the wave activity seen across the pores arises from the same physical source, the phase differences between LOS velocity, LOS magnetic field, geometrical height and temperature oscillations across all pores were calculated in a pair-wise fashion using a wavelet cross-correlation approach.

To rule out potential false signals due to incoherent oscillations within the pores, the pores with non-vanishing permanent areas were chosen for further pixel-by-pixel analysis. Phase differences in coherent velocity and magnetic field oscillations between the barycentric pixel and all other constant pixels were obtained using a Morlet coherence-wavelet transform with the same parameters as outlined above, with period greater than $T/3\sqrt{2}$ neglected. The resulting histograms for the phase lags within the pores (Figure 5) display a largely normal distribution and are roughly concentrated on zero, for both $B_{\rm LOS}$ and ^{v}LOS signals, indicating that the oscillations within pores are largely coherent. However, both distributions are quite broad, which may suggest that the signals, potentially containing real magnetic oscillations, are being contaminated by a separate source.

To check if any opacity effects are tainting the signals, we conducted a phase difference analysis of the $B_{\rm LOS}$ against other parameters, including geometrical height and temperature using Welch's method. Figure 6 displays the phase difference between $B_{\rm LOS}$ and geometric height z, temperature and ^{v}LOS for pore 9 at the $\log(\tau) = -1$ level. This plot displays the full signals, however, only the frequencies which are above a 0.8 high coherence threshold are displayed as the solid lines marked with crosses. Interestingly, at higher frequency waves (> 6 mHz) the phase difference plateaus around 0° for the $B_{\rm LOS}$ vs. geometrical height analysis, which suggests that these waves are not a result of opacity effects. On the other hand, the lower frequencies (< 6 mHz) display an anti-phase/more random phase relationship, which may be a result of opacity effects.

Figure 7 displays the phase difference, in radians, of different parameters $B_{\rm LOS}$, plasma temperature, geometrical height and ^{v}LOS in pore 9 at two different inversion levels, at $\log(\tau) = -1$ and $\log(\tau) = -2$. For the majority of frequencies, there is an in-phase relationship between the different levels, especially for the inferred geometrical

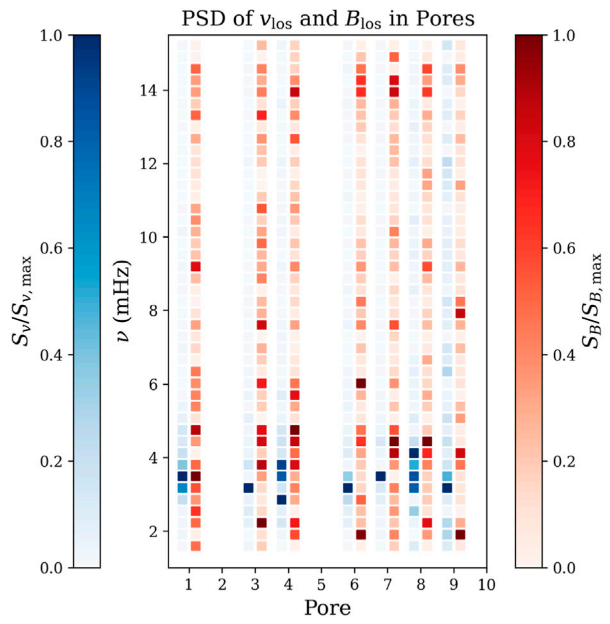

FIGURE 4
Normalised power spectral density as calculated from the detrended and apodised ^{v}LOS (blue) and $B_{\rm LOS}$ (red) time series for each of the pores. In the former, the 3 mHz photospheric oscillations dominate the PSD.

height which displays coherent zero phase lag at all frequencies. This suggests that the height scale from the inversions is stationary and that structures within the FoV move together coherently. At higher frequencies (> 6 mHz) there is a mainly positive phase difference in the line of sight velocity from the different $\log(\tau)$ levels. Given that $\log(\tau) = -2$ corresponds to a formation height higher up in the atmosphere, we can conclude that there is upward wave propagation at these higher frequencies. It could be argued that the temperature displays similar behaviour which would suggest a coupling between the ^{v}LOS and temperature, indicative of upward propagating slow magnetoacoustic waves.

It is worth noting that the anti-phase behaviour observed at low frequencies between $B_{\rm LOS}$ and geometric height is not uniquely attributable to opacity effects. Alternative explanations include height-dependent wave propagation delays, contributions from different magnetoacoustic wave modes, and asymmetries in the SIR inversion response functions. However, if the anti-phase $B_{\rm LOS}$ vs. z behaviour at low frequencies were due to a real propagating wave, one would expect a corresponding inter-layer phase lag in $B_{\rm LOS}$ between $\log(\tau) = -1$ and $\log(\tau) = -2$, analogous to the upward propagation signature clearly seen in ^{v}LOS at high frequencies. The absence of such a lag at low frequencies, seen in Figure 7, where $B_{\rm LOS}$, temperature and ^{v}LOS remain largely in-phase between the two inversion levels, is more consistent with a common, height-independent source such as an opacity-driven formation height shift than with genuine wave activity. Nonetheless, standing or evanescent oscillations below the acoustic cut-off would also create negligible inter-layer lags, and a conclusive determination would require dedicated forward modelling or response function analysis.

3.3 Coherence

To further determine whether opacity effects are present in the inversion data, we analyse the coherence and phase relationship between the signals $B_{\rm LOS}$ and geometric height z. To understand the correlation between the observed $B_{\rm LOS}$ oscillations and variations in z, given that we expect $B_{\rm LOS}$ to decrease with height, then opacity-induced $B_{\rm LOS}$ fluctuations would show a negative correlation with height. However, if instead there is a positive correlation between $B_{\rm LOS}$ and z, as reported in Joshi and de la Cruz Rodríguez (2018), that would suggest that the $B_{\rm LOS}$ oscillations are real, and not just due to the formation height shifting (i.e., not due to opacity effect). Given the quasi-periodic nature of these signals, we adopt a wavelet coherence analysis showing when and at which frequencies the coherence is significant. The temporal information could be key to better understanding the physical origin of the observed oscillations. To conduct a wavelet analysis, a 7×7 pixel square around the central pixel of the pore (i.e., 3 pixels above, below, left and right) were used to create an average signal used for phase analysis.

Figure 8 displays the wavelet analysis between $B_{\rm LOS}$ and height at $\log(\tau) = -1$ for a selection of pores. It is evident that there are a range of coherent frequencies present in both signals, however there is a strong in-phase relationship at higher frequencies, i.e., frequencies above 6 mHz (periods below ≈160 s). Given the quasi-periodic nature of the signals, the in-phase relationship of higher frequencies is stronger towards the end of the observation, for times later than 1,500 s. This in phase behaviour is expected for real signatures of MHD wave propagation to the chromosphere (Joshi and de la Cruz Rodríguez, 2018). On the other hand, the lower frequencies, typical of p-modes, generally display an anti-phase nature between $B_{\rm LOS}$ and height, which is expected if opacity effects are contaminating the signals. Therefore, we can imply that the high-frequency signals appear to be true oscillations. However, the lower (< 3 mHz) frequencies may be enmeshed with opacity effects, a conclusion which was also drawn by Grant et al. (2022) where, in their study, the higher frequencies seen in the chromosphere were not coherent.

To isolate the coherent frequencies, a similar cross-wavelet analysis between $B_{\rm LOS}$ and z was conducted using WaLSAtools (Jafarzadeh et al., 2025) for pore 8. Figure 9 displays the coherent phases, for two thresholds with coherence above 0.6 and above 0.8 respectively, as a function of frequency for the selected pore. The shaded region in Figure 9 highlights the circular standard deviation of the phase. This analysis further highlights the in-phase and anti-phase nature, of high (> 6 mHz) and low (<6 mHz) frequencies, respectively, when focusing on the coherent frequencies of the two signals. We also repeated the analysis for $\log(\tau) = -2$, as displayed in Figure 10. The same conclusion can be drawn from the behaviour of the signals at $\log(\tau) = -2$ for low and high frequencies. We emphasise that the 6 mHz division adopted here is an empirical threshold motivated by the change in phase/coherence behaviour seen in our data, rather than a universal physical cut-off. Frequencies above this value show phase signatures more consistent with upward-propagating magnetoacoustic disturbances, whereas below it the inferred $B_{\rm LOS}$ behaviour is more susceptible to opacity-related contamination.

Figure 11 displays histograms of coherent phase between $B_{\rm LOS}$ and z for pores 3, 4, 6, 7, 8 and 9 at $\log(\tau) = -1$. These histograms are

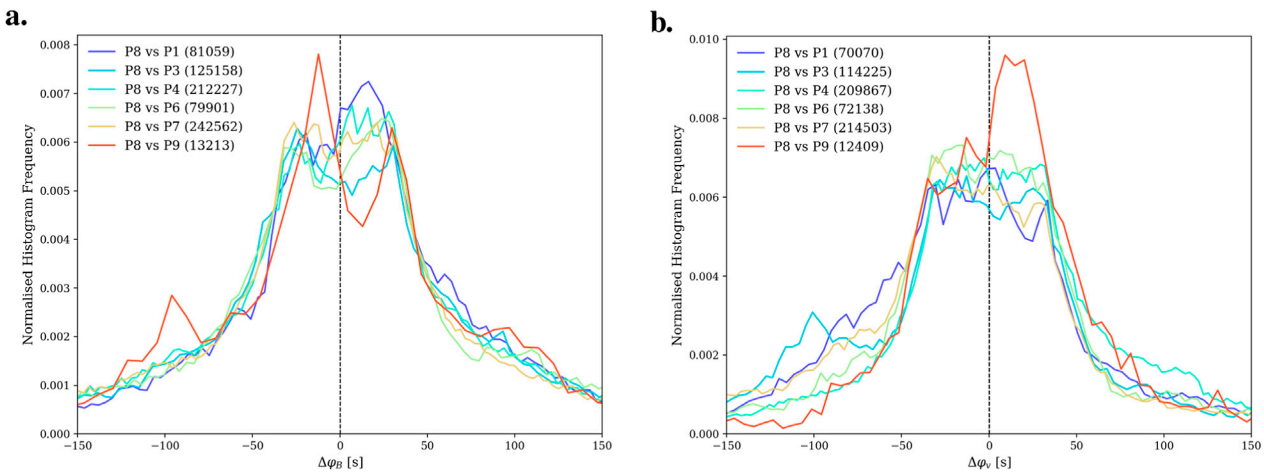

FIGURE 5
Distribution of phase differences, displayed as time lags, of the **(a)** B_{LOS} and **(b)** ^{v}LOS signals from pore 8 against the other pores considered in the analysis for $\log(\tau) = -1$.

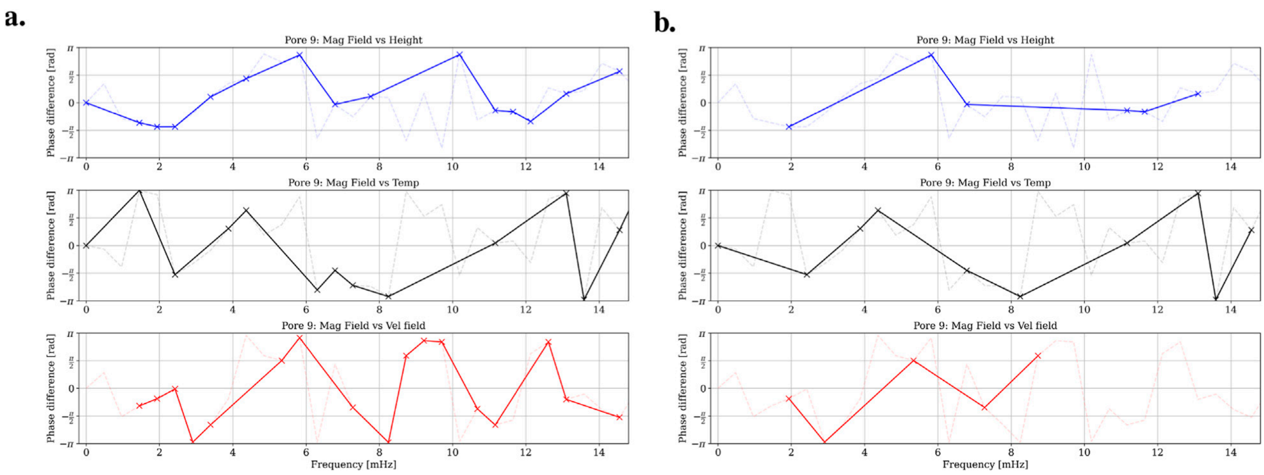

FIGURE 6
Phase difference of B_{LOS} against (top panel) geometric height z, (middle panel) temperature and (bottom panel) ^{v}LOS for pore 9 at $\log(\tau) = -1$. **(a)** Coherence threshold of 0.6. **(b)** Coherence threshold of 0.8. The coherent frequencies are marked with a cross and displayed with the solid line. The original signal is shown as the shaded dashed line.

essentially showing the same data denoted by the arrows outside the CoI in Figure 8 over time, reduced to a 1D array where information regarding the frequency of coherent phase is lost. The same phase distributions are shown in Figure 12 for $\log(\tau) = -2$. For pores 3, 6 and 7 there are clear peaks towards ±180°, suggestive of out-of-phase behaviour which indicates contamination of the signals from opacity effects. On the other hand, pore 8 displays an enhancement of phase around 0°. This behaviour in the phase analysis suggests the presence of real MHD waves. This is especially interesting as it is most pronounced in pore 8, which is also the most 'rounded' pore within the SST FoV (see Figure 1) which indicates this pore may be the most 'effective' waveguide. A similar conclusion can be drawn from the histograms of coherent phase at $\log(\tau) = -2$, highlighting the coherent behaviour across the different heights spanning the peak of the Fe I 6,301 Å line.

4 Conclusion

In this study, we have examined the oscillatory behaviour within a group of solar pores using photospheric spectropolarimetric observations from CRISP at the Swedish 1-m Solar Telescope. Through SIR inversions, we retrieved the line-of-sight velocity and magnetic field, revealing strong oscillatory power at typical photospheric periods (3–5 min), consistent with the solar p-mode spectrum (Lites et al., 1982).

10.3389/fspas.2026.1814323

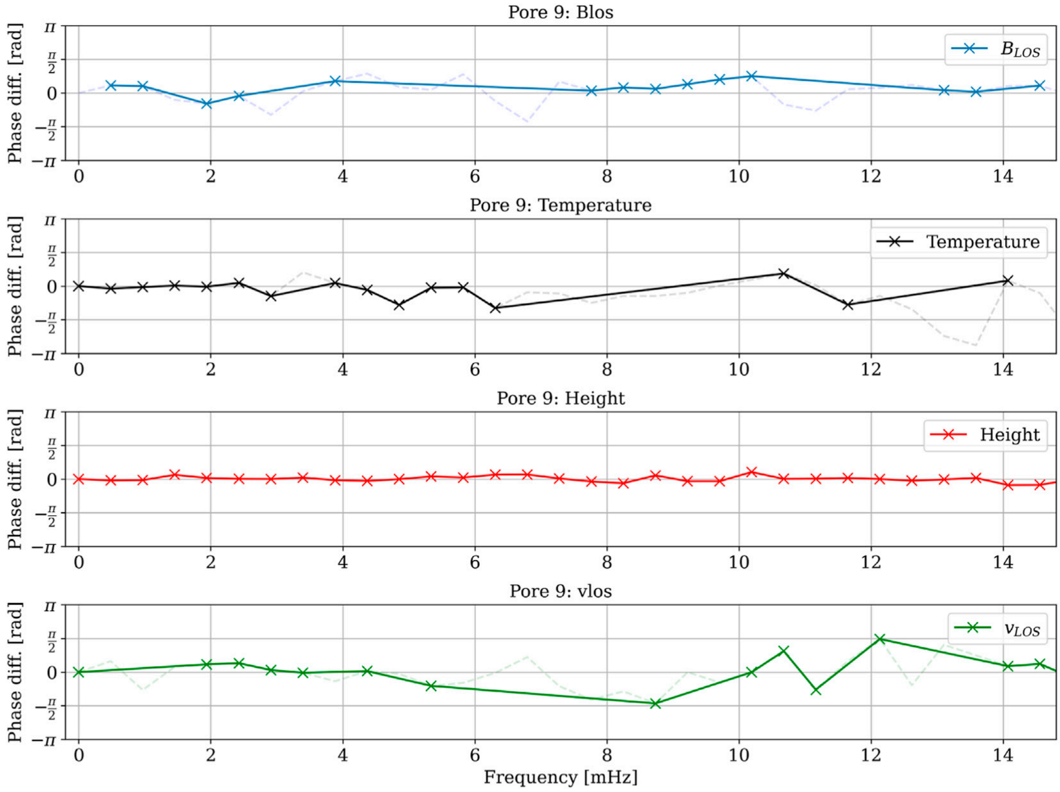

FIGURE 7
Phase difference between B_{LOS}, temperature, geometrical height and ^{v}LOS at log(τ) = −1 and log(τ) = −2 levels in Pore 9. The crosses indicate coherent frequencies in the analysis, shown with the solid line, the original signal is shown as the shaded dashed line.

By analysing the SIR inversion output at multiple $\log(\tau)$ levels, we investigated how variations in ^{v}LOS, B_{LOS}, temperature, and geometrical height are interrelated. At high frequencies (> 6 mHz), we find coherent, in-phase fluctuations between B_{LOS} and height. Additional phase analysis at $\log(\tau) = -1$ and $\log(\tau) = -2$ indicates signatures consistent with upward-propagating magnetoacoustic waves, supported by positive phase differences in both ^{v}LOS and temperature between these layers.

A coherence-wavelet comparison of B_{LOS} and geometric height across the pore ensemble reveals clear differences: coherence and in-phase behaviour at high frequencies, but significant phase offsets at lower frequencies (< 6 mHz). A similar behaviour is seen across all pores over the large FoV, indicating that this may be a global phenomenon, and not isolated to an individual pore. These discrepancies highlight a critical need to verify the physical origin of low-frequency magnetic oscillations in future magnetic surveys with facilities such as SUNRISE and DKIST. In particular, the 3 mHz magnetic oscillations inferred from spectropolarimetric inversions may be affected by opacity and this should be further scrutinised in future studies. Ground-based facilities are particularly well-suited for these investigations, as their larger apertures enable them to resolve individual pore structures and detect the subtle polarimetric signals associated with magnetic oscillations (e.g., Scharmer et al., 2019; Jess et al., 2023).

Our findings suggest that opacity effects may contaminate the observed spectropolarimetric oscillations. While the pores exhibit striking coherence in magnetic oscillations across large spatial separations, displaying coherent waveguide-like behaviour, our analysis indicates that, below 6 mHz, opacity variations may contaminate the measured signals and artificially enhance coherence, evidenced by the greater power in ^{v}LOS and B_{LOS} for frequencies below 6 mHz shown in Figure 2, in addition to the change in character about 6 mHz for the wavelet coherence analysis displayed in Figure 8. This may partially account for the prominence of 3 mHz power in previous studies, implying that the photospheric power distribution between 3 and 5 mHz may be more balanced than traditionally assumed. It is apparent that, at low frequencies below 3 − 4 mHz, there is a 180° phase difference between B_{LOS} and height perturbations, however, at higher frequencies, the phase between the signals tends towards 0°, indicative of magnetoacoustic wave phenomena.

The opacity-induced artefacts identified in this study have direct implications for numerical MHD simulations that aim to reproduce observed wave signatures in the solar atmosphere. Simulations that model wave propagation in flux tube geometries representative of waveguides in the lower solar atmosphere must account for the fact that spectropolarimetric inversions may not faithfully recover the underlying wave properties at low frequencies. In particular, simulations of slow magnetoacoustic wave propagation (e.g., Riedl et al., 2021; Yadav et al., 2021) and studies that forward-model Stokes diagnostics from MHD outputs (e.g., Felipe and Socas-Navarro, 2023) would benefit from incorporating opacity-driven

 10.3389/fspas.2026.1814323

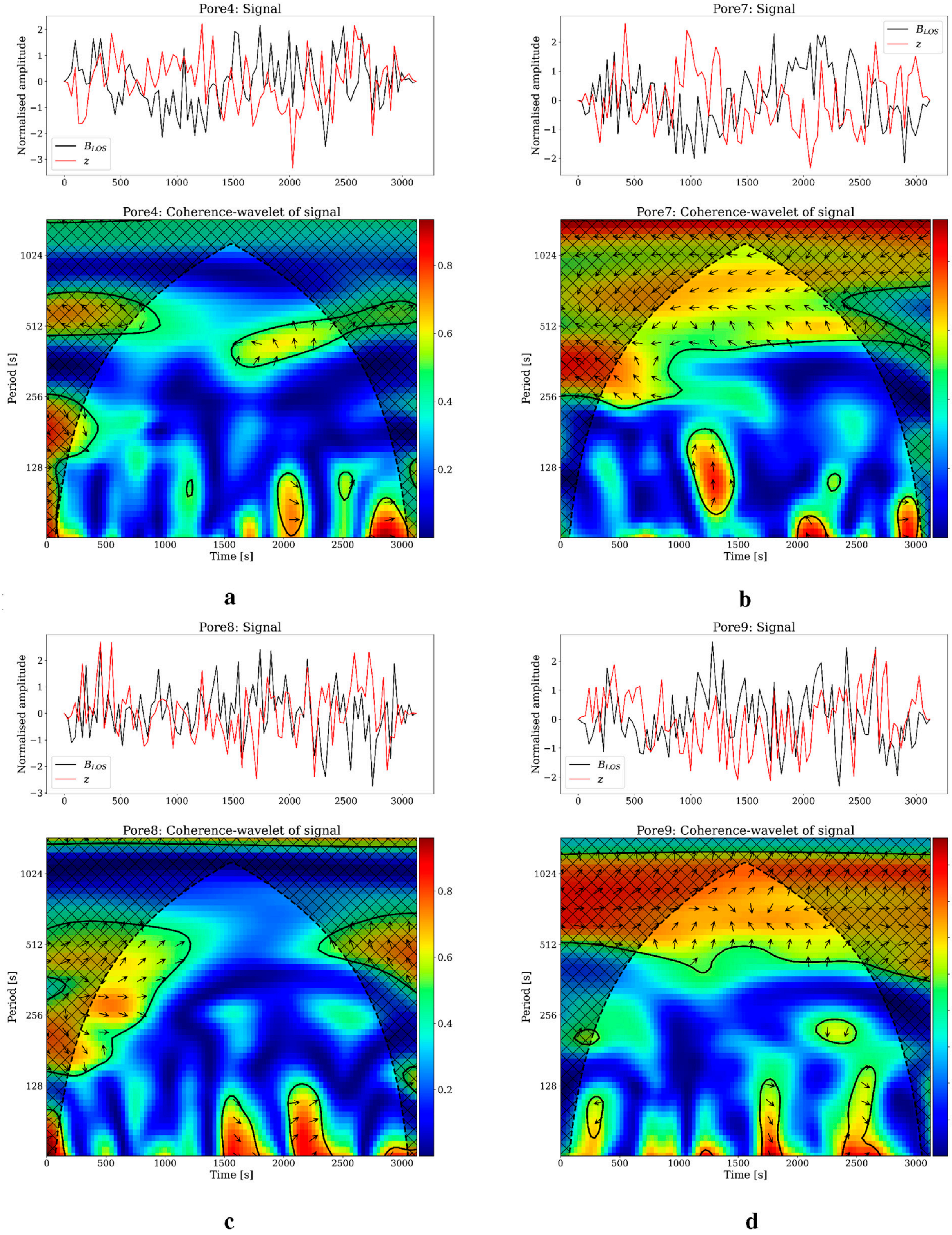

FIGURE 8
Wavelet coherence of B_{los} vs. height at $\log(\tau) = -1$ for **(a)** pore 4, **(b)** pore 7, **(c)** pore 8 and **(d)** pore 9. The top panel of each plot shows the detrended signals whereas the bottom panels display the coherence wavelet between the two signals. In the bottom panels, arrows indicate phase difference: 0° (right), 180° (left), 90° (up), and −90° (down).

10.3389/fspas.2026.1814323

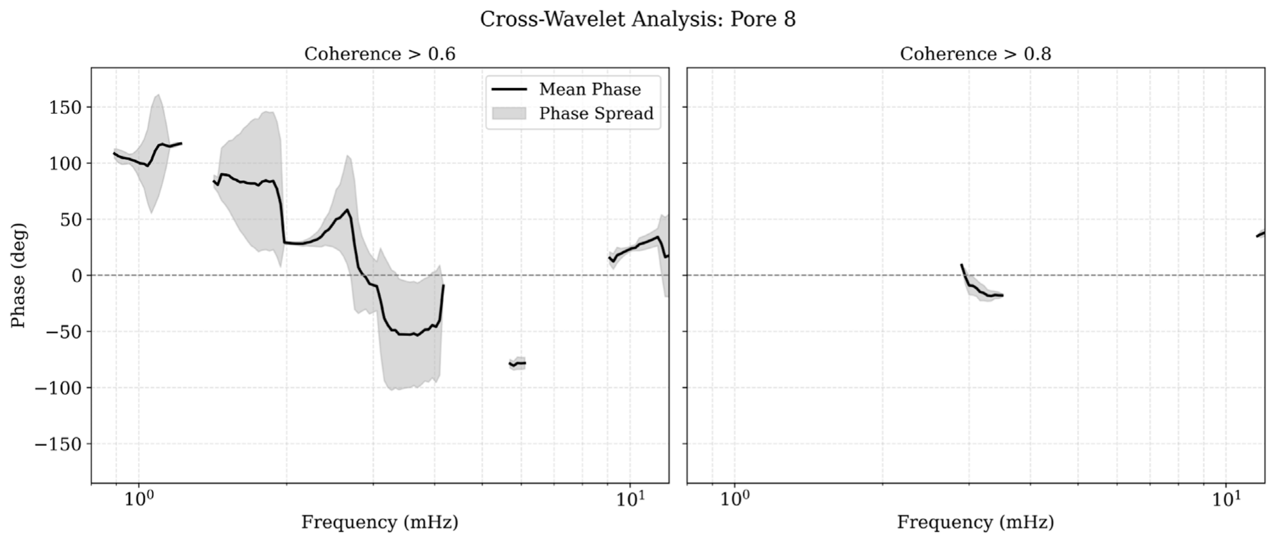

FIGURE 9
Coherent phase versus frequency analysis between B_{LOS} and height z, for pore 8 at $\log(\tau) = -1$. The left panel shows the relationship between frequencies with coherence > 0.6 whereas the right panel shows the phase vs. frequencies with coherence > 0.8. The phase spread determined using the circular standard deviation is shown as the shaded region.

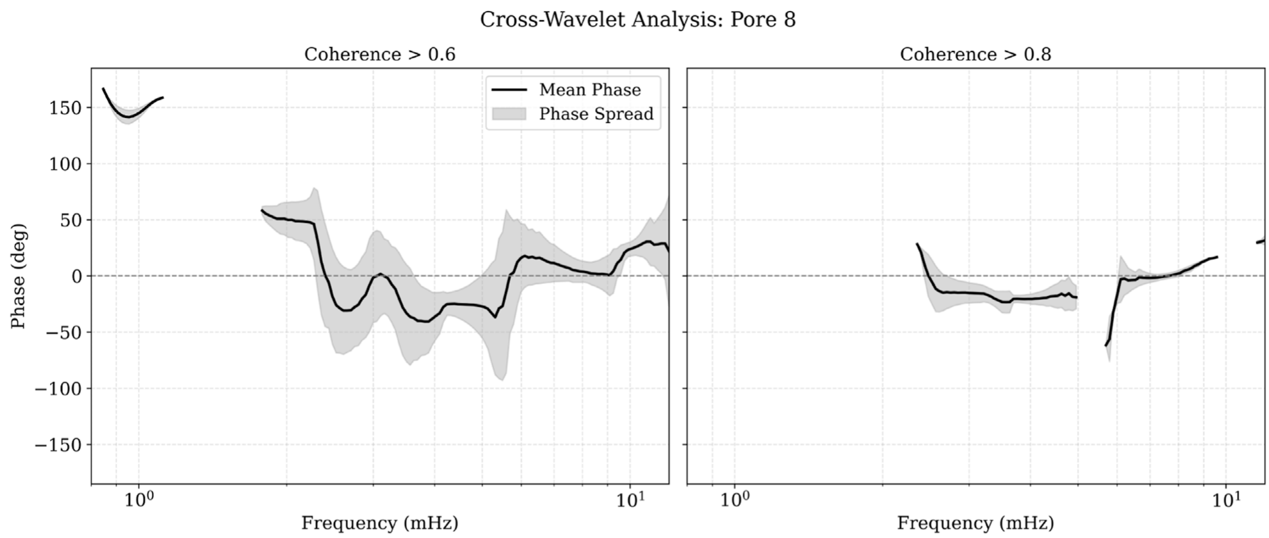

FIGURE 10
Same as Figure 9 for pore 8 but for $\log(\tau) = -2$.

response function effects when comparing synthetic observables to real data.

To conclusively determine the extent to which opacity contributes to apparent magnetic and velocity oscillations in the lower solar atmosphere, future observational efforts must be complemented by realistic 3D numerical simulations and full radiative forward modelling. Such work will be essential to disentangle genuine MHD wave signatures from opacity-induced artefacts and to refine the interpretation of high-resolution solar magnetic diagnostics. This is vital in terms of accurately diagnosing the energy transported by MHD waves across various layers in the solar atmosphere.

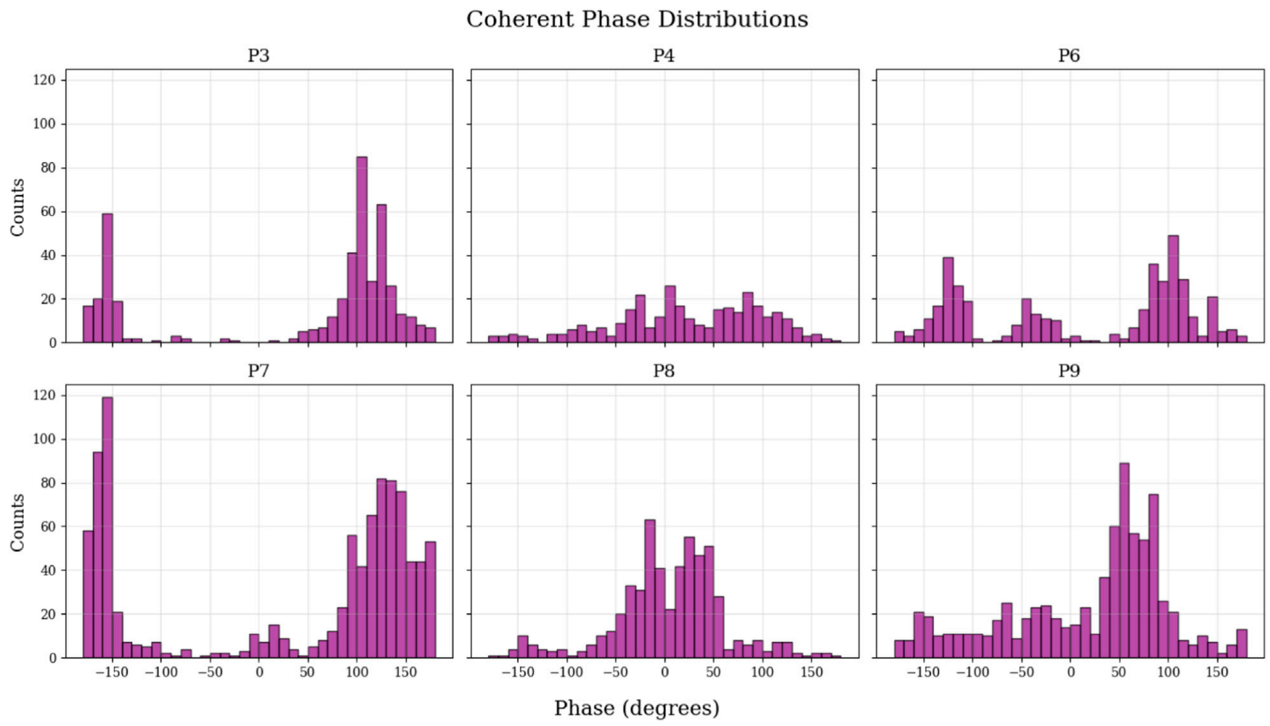

FIGURE 11
Histograms for the coherent phases (in degrees) between B_{LOS} and z within a selection of pores from the inversions at $\log(\tau) = -1$.

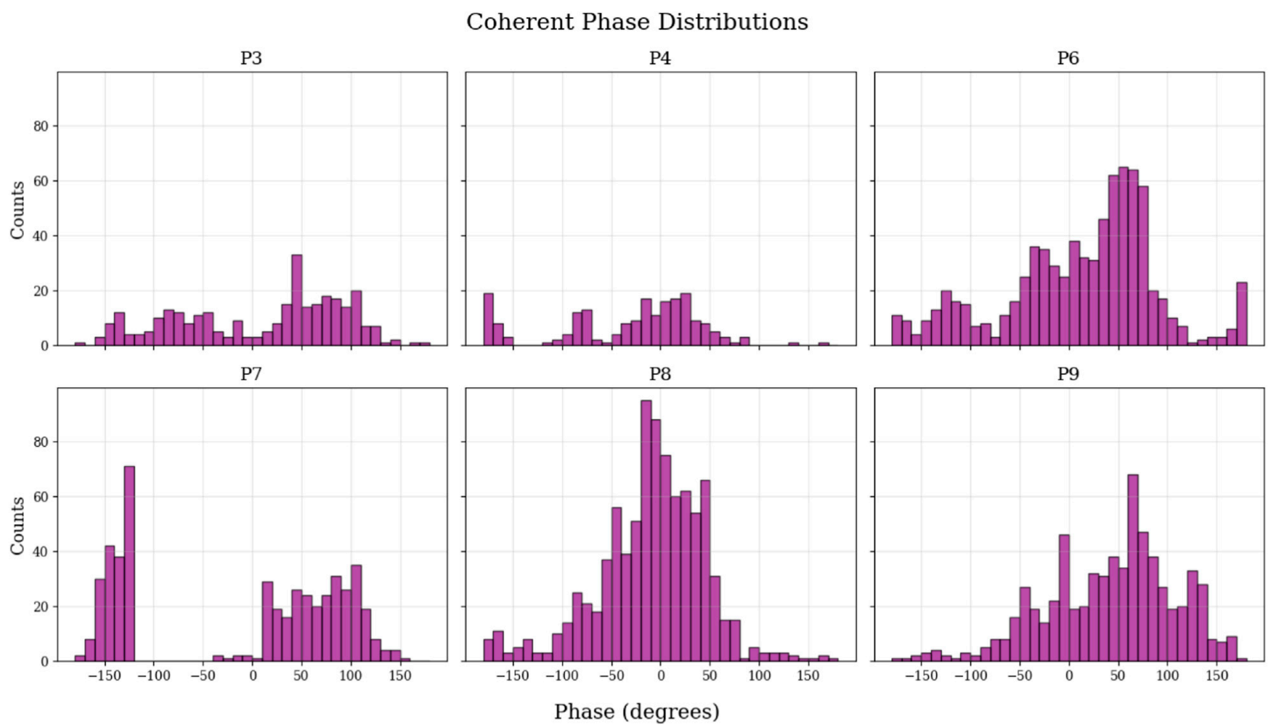

FIGURE 12
Same as Figure 11 but for $\log(\tau) = -2$.

Data availability statement

The raw data supporting the conclusions of this article will be made available by the authors, without undue reservation.

Author contributions

SS: Conceptualization, Data curation, Formal Analysis, Investigation, Methodology, Validation, Visualization, Writing – original draft, Writing – review and editing. SG: Conceptualization, Data curation, Funding acquisition, Methodology, Project administration, Resources, Supervision, Writing – review and editing. DJ: Funding acquisition, Methodology, Project administration, Supervision, Writing – review and editing. RC: Data curation, Formal Analysis, Methodology, Writing – review and editing. SJ: Methodology, Supervision, Writing – review and editing. MK: Data curation, Formal Analysis, Methodology, Writing – review and editing. MB: Data curation, Resources, Writing – review and editing. TD: Investigation, Methodology, Writing – review and editing. GC: Data curation, Writing – review and editing. MS: Data curation, Resources, Writing – review and editing. LR: Data curation, Resources, Writing – review and editing.

Funding

The author(s) declared that financial support was received for this work and/or its publication. S.J.S acknowledges support from the UKRI Future Leader Fellowship Grant (RiPSAW MR/Z000289/1). S.J.S., S.D.T.G., D.B.J., S.J. and T.J.D. are grateful to the UK STFC for the consolidated grants ST/T00021X/1 and ST/X000923/1. S.J. acknowledges support from the European Research Council under the European Union Horizon 2020 research and innovation program (grant agreement No. 682462) and from the Research Council of Norway through its Centres of Excellence scheme (project No. 262622).

Acknowledgements

We wish to acknowledge scientific discussions with the Waves in the Lower Solar Atmosphere (WaLSA; www.WaLSA.team) team, which has been supported by the Research Council of Norway (project no. 262622), The Royal Society (award no. Hooke18b/SCTM; Jess et al., 2021), and the International Space Science Institute (ISSI) in Bern through ISSI International Team project 502 "WaLSA: Waves in the Lower Solar Atmosphere at High Resolution".

Conflict of interest

The author(s) declared that this work was conducted in the absence of any commercial or financial relationships that could be construed as a potential conflict of interest.

Generative AI statement

The author(s) declared that generative AI was not used in the creation of this manuscript.

Any alternative text (alt text) provided alongside figures in this article has been generated by Frontiers with the support of artificial intelligence and reasonable efforts have been made to ensure accuracy, including review by the authors wherever possible. If you identify any issues, please contact us.

Publisher's note

References

Asplund, M., Grevesse, N., Sauval, A. J., and Scott, P. (2009). The chemical composition of the sun. *arXiv* 47, 481–522. doi:10.1146/annurev.astro.46.060407.145222

Bailén, F. J., Orozco Suárez, D., and del Toro Iniesta, J. C. (2023). Fabry-pérot etalons in solar astronomy. A review. *Astrophysics Space Sci.* 368, 55. doi:10.1007/s10509-023-04212-3

Campos Rozo, J. I., Vargas Domínguez, S., Utz, D., Veronig, A. M., and Hanslmeier, A. (2023). Exploring magnetic field properties at the boundary of solar pores: a comparative study based on SDO-HMI observations. *Astronomy and Astrophysics* 674, A91. doi:10.1051/0004-6361/202346389

de la Cruz Rodríguez, J., and van Noort, M. (2017). Radiative diagnostics in the solar photosphere and chromosphere. *Space Sci. Rev.* 210, 109–143. doi:10.1007/s11214-016-0294-8

de la Cruz Rodríguez, J., Löfdahl, M. G., Sütterlin, P., Hillberg, T., and Rouppe van der Voort, L. (2015). CRISPRED: a data pipeline for the CRISP imaging spectropolarimeter. *Astronomy and Astrophysics* 573, A40. doi:10.1051/0004-6361/201424319

Dorotovič, I., Erdélyi, R., and Karlovský, V. (2008). Identification of linear slow sausage waves in magnetic pores. In *Proc Int Astron Union, Waves and Oscillations Sol Atmos Heat Magneto-Seismology*, eds R. Erdélyi, and C. A. Mendoza-Briceno 247, 351–354. doi:10.1017/S174392130801507X

Felipe, T., and Socas-Navarro, H. (2023). Impact of opacity effects on chromospheric oscillations inferred from NLTE inversions. *Astronomy and Astrophysics* 670, A133. doi:10.1051/0004-6361/202245439

Fujimura, D., and Tsuneta, S. (2009). Properties of magnetohydrodynamic waves in the solar photosphere obtained with hinode. *Astrophysical J.* 702, 1443–1457. doi:10.1088/0004-637X/702/2/1443

Garcia de La Rosa, J. I. (1987). Umbral dots - a case of penetrative convection between sunspot fragments. *Sol. Phys.* 112, 49–58. doi:10.1007/BF00148486

Gilchrist-Millar, C. A., Jess, D. B., Grant, S. D. T., Keys, P. H. K., Beck, C., Jafarzadeh, S., et al. (2021). Magnetoacoustic wave energy dissipation in the atmosphere of solar pores. *Philosophical Trans. R. Soc. Lond. Ser. A* 379, 20200172. doi:10.1098/rsta.2020.0172

Grant, S. D. T., Jess, D. B., Moreels, M. G., Morton, R. J., Christian, D. J., Giagkiozis, I., et al. (2015). Wave damping observed in upwardly propagating sausage-mode oscillations contained within a magnetic pore. *Astrophysical J.* 806, 132. doi:10.1088/0004-637X/806/1/132

Grant, S. D. T., Jess, D. B., Stangalini, M., Jafarzadeh, S., Fedun, V., Verth, G., et al. (2022). The propagation of coherent waves across multiple solar magnetic pores. *Astrophysical J.* 938, 143. doi:10.3847/1538-4357/ac91ca

Houston, S. J., Jess, D. B., Asensio Ramos, A., Grant, S. D. T., Beck, C., Norton, A. A., et al. (2018). The magnetic response of the solar atmosphere to umbral flashes. *Astrophysical J.* 860, 28. doi:10.3847/1538-4357/aab366

Jafarzadeh, S., Schiavo, L. A. C. A., Fedun, V., Solanki, S. K., Stangalini, M., Calchetti, D., et al. (2024). Sausage, kink, and fluting magnetohydrodynamic wave modes identified in solar magnetic pores by solar Orbiter/PHI. *Astronomy and Astrophysics* 688, A2. doi:10.1051/0004-6361/202449685

Jafarzadeh, S., Jess, D. B., Stangalini, M., Grant, S. D. T., Higham, J. E., Pessah, M. E., et al. (2025). Wave analysis tools. *Nat. Rev. Methods Prim.* 5, 21. doi:10.1038/s43586-025-00392-0

Jess, D. B., Morton, R. J., Verth, G., Fedun, V., Grant, S. D. T., and Giagkiozis, I. (2015). Multiwavelength studies of MHD waves in the solar chromosphere. An overview of recent results. *Space Sci. Rev.* 190, 103–161. doi:10.1007/s11214-015-0141-3

Jess, D. B., Keys, P. H., Stangalini, M., and Jafarzadeh, S. (2021). High-resolution wave dynamics in the lower solar atmosphere. *Philosophical Trans. R. Soc. Lond. Ser. A* 379, 20200169. doi:10.1098/rsta.2020.0169

Jess, D. B., Jafarzadeh, S., Keys, P. H., Stangalini, M., Verth, G., and Grant, S. D. T. (2023). Waves in the lower solar atmosphere: the dawn of next-generation solar telescopes. *Living Rev. Sol. Phys.* 20, 1. doi:10.1007/s41116-022-00035-6

Joshi, J., and de la Cruz Rodríguez, J. (2018). Magnetic field variations associated with umbral flashes and penumbral waves. *Astronomy and Astrophysics* 619, A63. doi:10.1051/0004-6361/201832955

Keys, P. H., Morton, R. J., Jess, D. B., Verth, G., Grant, S. D. T., Mathioudakis, M., et al. (2018). Photospheric observations of surface and body modes in solar magnetic pores. *Astrophysical J.* 857, 28. doi:10.3847/1538-4357/aab432

Lites, B. W., White, O. R., and Packman, D. (1982). Photoelectric observations of propagating sunspot oscillations. *Astrophysical J.* 253, 386–392. doi:10.1086/159642

Morton, R. J., Erdélyi, R., Jess, D. B., and Mathioudakis, M. (2011). Observations of sausage modes in magnetic pores. *Astrophysical J. Lett.* 729, L18. doi:10.1088/2041-8205/729/2/L18

Morton, R. J., Sharma, R., Tajfirouze, E., and Miriyala, H. (2023). Alfvénic waves in the inhomogeneous solar atmosphere. *Rev. Mod. Plasma Phys.* 7, 17. doi:10.1007/s41614-023-00118-3

Murabito, M., Stangalini, M., Baker, D., Valori, G., Jess, D. B., Jafarzadeh, S., et al. (2021). Investigating the origin of magnetic perturbations associated with the FIP effect. *Astronomy and Astrophysics* 656, A87. doi:10.1051/0004-6361/202141504

Nelson, C. J., Campbell, R. J., and Mathioudakis, M. (2021). Oscillations in the line-of-sight magnetic field strength in a pore observed by the GREGOR infrared spectrograph (GRIS). *Astronomy and Astrophysics* 654, A50. doi:10.1051/0004-6361/202141368

Quintero Noda, C., Barklem, P. S., Gafeira, R., Ruiz Cobo, B., Collados, M., Carlsson, M., et al. (2021). Diagnostic capabilities of spectropolarimetric observations for understanding solar phenomena. *I. Zeeman-Sensitive Photospheric Lines* 652, A161. doi:10.1051/0004-6361/202037735

Riedl, J. M., Gilchrist-Millar, C. A., Van Doorsselaere, T., Jess, D. B., and Grant, S. D. T. (2021). Finding the mechanism of wave energy flux damping in solar pores using numerical simulations. *Astronomy and Astrophysics* 648, A77. doi:10.1051/0004-6361/202040163

Ruiz Cobo, B., and del Toro Iniesta, J. C. (1992). Inversion of stokes profiles. *Astrophysical J.* 398, 375. doi:10.1086/171862

Scharmer, G. B., Bjelksjo, K., Korhonen, T. K., Lindberg, B., and Petterson, B. (2003). "The 1-meter Swedish solar telescope," in *Innovative Telescopes and Instrumentation for Solar Astrophysics*. Editors S. L. Keil, and S. V. Avakyan, 4853, 341–350. doi:10.1117/12.460377

Scharmer, G. B., Narayan, G., Hillberg, T., de la Cruz Rodriguez, J., Löfdahl, M. G., Kiselman, D., et al. (2008). CRISP spectropolarimetric imaging of penumbral fine structure. *Astrophysical J. Lett.* 689, L69–L72. doi:10.1086/595744

Scharmer, G. B., Löfdahl, M. G., Sliepen, G., and de la Cruz Rodríguez, J. (2019). Is the sky the limit? Performance of the revamped Swedish 1-m solar telescope and its blue- and red-beam reimaging systems. *Astronomy and Astrophysics* 626, A55. doi:10.1051/0004-6361/201935735

Sobotka, M. (2003). Solar activity II: sunspots and pores. *Astron. Nachrichten* 324, 369–373. doi:10.1002/asna.200310132

Stangalini, M., Baker, D., Valori, G., Jess, D. B., Jafarzadeh, S., Murabito, M., et al. (2021a). Spectropolarimetric fluctuations in a sunspot chromosphere. *Philosophical Trans. R. Soc. Lond. Ser. A* 379, 20200216. doi:10.1098/rsta.2020.0216

Stangalini, M., Jess, D. B., Verth, G., Fedun, V., Fleck, B., Jafarzadeh, S., et al. (2021b). A novel approach to identify resonant MHD wave modes in solar pores and sunspot umbrae: $b-\omega$ analysis. *Astronomy and Astrophysics* 649, A169. doi:10.1051/0004-6361/202140429

Sui, W., and Zhang, D. (2012). Four methods for roundness evaluation. *Phys. Procedia* 24, 2159–2164. doi:10.1016/j.phpro.2012.02.317

Torrence, C., and Compo, G. P. (1998). A practical guide to wavelet analysis. *Bull. Am. Meteorological Soc.* 79, 61–78. doi:10.1175/1520-0477(1998)079⟨0061:APGTWA⟩2.0.CO;2

Van Doorsselaere, T., Srivastava, A. K., Antolin, P., Magyar, N., Vasheghani Farahani, S., Tian, H., et al. (2020). Coronal heating by MHD waves. *Space Sci. Rev.* 216, 140. doi:10.1007/s11214-020-00770-y

Van Noort, M., Rouppe Van Der Voort, L., and Löfdahl, M. G. (2005). Solar image restoration by use of multi-frame blind De-convolution with multiple objects and phase diversity. *Sol. Phys.* 228, 191–215. doi:10.1007/s11207-005-5782-z

Yadav, N., Cameron, R. H., and Solanki, S. K. (2021). Slow magneto-acoustic waves in simulations of a solar plage region carry enough energy to heat the chromosphere. *arXiv* 652, A43. doi:10.1051/0004-6361/202039908